JOURNAL OF COMPUTATIONAL PHYSICS **120,** 171–183 (1995)

A Spectral Time Discretization for Flows with Dominant Periodicity

GILLES CARTE*, AND JAN DUŠEK†

Institut de Mécanique Statistique de la Turbulence, 12, Avenue du Général Leclerc, 13003 Marseille, France

AND

PHILIPPE FRAUNIÉ‡

LSEET, Université de Toulon et du Var, B. P. 132, 83957 La Garde, Cedex, France

Received August 5, 1994; revised January 19, 1995

An accurate and efficient treatment of periodic and quasi-periodic flows based on the temporal Fourier decomposition of the Navier–Stokes equations is suggested. A numerical implementation for a laminar afterbody wake in a 2D channel is presented. This implementation is formulated in primitive variables and uses an ordinary second-order accurate finite volume space discretization combined with a standard pressure correction procedure. A multistep time marching scheme for numerical and physical transients is developed. For flows with a variable dominant period, a period correction algorithm is used. The transients characterizing the instability development are simulated. The numerical results obtained for the afterbody wake confirm the expectations concerning the efficiency and high time accuracy of the method. Moreover, the method provides direct access to quantities difficult to obtain by other methods such as the envelope and the angular velocity variation of the unstable mode.

1. INTRODUCTION

A substantial progress in the understanding of the onset of instabilities in wakes has been achieved thanks to accurate numerical simulations ([1] and references therein). It appears that not only in wakes but in most cases of unstable configurations such as parallel flows [2], boundary layers [3], and jets [4] the onset of the primary instability corresponds to a Hopf bifurcation [5] accompanied by a transition from a steady to an unsteady periodic flow. A series of experimental [4, 6, 7] and numerical investigations [1] have confirmed that the Hopf bifurcation can be locally described by the Landau model [8]. The Hopf bifurcation is characterized by flow oscillations with a slowly varying dominant frequency and by a transient modulation of the oscillation amplitudes. The most relevant features of the bifurcation are related to the transients, i.e., to the envelope of the oscillations and to the shift of the Strouhal frequency. Moreover, the latest results show [1, 9] that the spatial structure of the instability presents a special interest.

Numerical 2D and 3D [10, 11] simulations of laminar wakes show that the time and space characteristics of the Hopf bifurcation can be, in principle, simulated with a sufficient accuracy to obtain a good agreement with experimental data. It appears, however, that especially in 3D serious trade-offs have to be made as far as the accuracy of computations is concerned due to the necessity to reduce the computing costs in order to be able to obtain sufficiently long temporal data. In the case of 2D computations, numerical investigation of such a simple configuration as two interacting cylinder wakes becomes simply prohibitive because the time scale of the beatings of the interacting wakes represents several tens of Strouhal periods. The same situation can be expected in fully 3D configurations, where there seems to be experimental evidence [12] of the onset of a secondary Benjamin–Feir-like instability leading, again, to rather slow beatings. It is easy to see that the high computing costs of simulations of the mentioned flows are related to the time marching resolution of the Navier–Stokes equations and to the necessity to recompute anew every new period even if the overall variation of the flow field from one period to the other is small. The stability constraints and time accuracy of the current solvers usually require large numbers of time steps per one basic (Strouhal) period (hundreds to thousands of time steps) just to reproduce almost the same quasi periodic behaviour many times. (Typically 50 to 100 periods are required to obtain an accurate analysis of the transients of the Bénard–von Kármán instability [1].)

Recently, a significant number of papers with numerical topics have been focussed on simulation of unsteady laminar flows.

* E-mail: carte@marius.univ-mrs.fr.

† On leave from the Institute of Thermomechanics, Academy of Sciences of the Czech Republic, Dolejškova 5, 182 00 Prague, Czech Republic. E-mail: dusek@marius.univ-mrs.fr.

‡ E-mail: fraunie@lseet.univ-tln.fr.

0021-9991/95 $12.00

The principal objectives of these papers is the improvement of the efficiency and accuracy of the spatial discretization: low order finite volume methods [13–15], high order finite difference [16, 17], spectral element methods [1, 11], or spectral methods [18]. However, the time discretization always consists in time marching techniques of varying order [19, 20] presenting for periodic and quasi periodic flows, the inconvenients exposed above.

A qualitatively different situation occurs in turbulent flows with dominant periodicity. This periodicity may be either forced or self-generated as is the case of turbulent wakes. It is well known that the von Kármán vortex street is very stable and a practically constant dominant Strouhal frequency is present until very high Reynolds numbers. Such turbulent flows are incompatible with the concept of time averaging in turbulence modelling and represent thus a real challenge [21]. It can be seen that the modelling problem arises from the necessity to separate the periodic oscillations (representing, this time, slow time scales) from the turbulent fluctuations and to introduce an alternative averaging concept.

In the present paper we propose a numerical method promising to provide a basis for solving the mentioned problems. Our considerations and test cases will concern mainly the simulation of slow time-scales in laminar wakes. In Section 2 we provide the theoretical basis of the method. In Section 3 we present the numerical implementation. The numerical results and comparisons with the standard time marching approach will be provided in Section 4.

2. THEORETICAL BACKGROUND

2.1. Governing Equations

We consider the Navier–Stokes equations for incompressible and viscous flows in the velocity–pressure formulation,

$$\frac{\partial \mathbf{v}}{\partial t} + \mathbf{v}\nabla\mathbf{v} - \nu\nabla^2\mathbf{v} + \nabla p = 0 \tag{1}$$

$$\nabla \cdot \mathbf{v} = 0, \tag{2}$$

where $\mathbf{v}$ denotes the velocity vector and p is the pressure. These equations have to be completed by boundary and initial conditions, which will be discussed in the next section. In order to simplify the presentation of our method let us remark that most methods of resolution of the set of Eqs. (1) and (2) written in the velocity–pressure formulation take account of the continuity equation (2) via some pressure correction method. The pressure correction amounts to replacing the continuity equation (2) by the pressure equation:

$$\nabla^2 p + \frac{\partial v_j}{\partial x_i}\frac{\partial v_i}{\partial x_j} = 0 \tag{3}$$

which is used at each time-step to obtain the correct pressure field. Let us symbolize the resolution of the pressure Poisson equation as

$$p = -(\nabla^2)^{-1}\frac{\partial v_j}{\partial x_i}\frac{\partial v_i}{\partial x_j}. \tag{4}$$

Equation (4) shows that the pressure term in Eq. (1) contributes to the nonlinearities of the equations. In this paper, we shall be mostly concerned with the aspects of the time dicretization of the Navier–Stokes equations. We shall therefore simplify the notation by introducing the (time-independent) nonlinear operator

$$\mathbf{F}(\mathbf{v}) \equiv -\nu\nabla^2\mathbf{v} + \mathbf{B}(\mathbf{v}, \mathbf{v}), \tag{5}$$

where $\mathbf{B}$ is the bilinear operator

$$\mathbf{B}(\mathbf{v}, \mathbf{w})_i = v_j\frac{\partial w_i}{\partial x_j} - \frac{\partial}{\partial x_i}(\nabla^2)^{-1}\frac{\partial v_j}{\partial x_k}\frac{\partial w_k}{\partial x_j}. \tag{6}$$

We thus arrive at the following formulation of Eqs. (1) and (2)

$$\frac{\partial \mathbf{v}}{\partial t} + F(\mathbf{v}) = 0. \tag{7}$$

The initial condition (to be discussed later) will be written as

$$\mathbf{v}(0, \cdot) = \mathbf{g}(\cdot). \tag{8}$$

(In what follows, we replace all the spatial variables by a point.)

2.2. Separation of Periodic Oscillations

Let us consider instead of Eq. (7) the equation

$$\frac{\partial \mathbf{u}}{\partial s} + \frac{\partial \mathbf{u}}{\partial t} + F(\mathbf{u}) = 0, \tag{9}$$

for $s \in [0, \infty[$ and $t \in [0, \infty[$ with the initial condition

$$\mathbf{u}(0, t, \cdot) = \mathbf{h}(t, \cdot) \tag{10}$$

where $\mathbf{h}(t, \cdot)$ is a given t-dependent field.

It is easy to see that if

$$\mathbf{h}(0, \cdot) = \mathbf{g}(\cdot)$$

and $\mathbf{u}$ is a solution of (9), (10) then

$$\mathbf{v}(t, \cdot) \equiv \mathbf{u}(t, t, \cdot) \tag{11}$$

is a solution of (7), (8). (We set $s = t$.)

The additional degree of freedom described by the variable s can be used to impose an arbitrary t-dependence of $\mathbf{u}$; the initial condition (10) includes an initial guess of the t-behaviour. In our case we shall set $\mathbf{u}$ periodic with a given period T as a function of t:

$$\mathbf{u}(s, t + T, \cdot) = \mathbf{u}(s, t, \cdot). \tag{12}$$

Accordingly, we shall assume the function h in (10) to be periodic with the same period. From what has been said above it is clear that, having solved Eqs. (9), (10), this does not prevent us to describe general nonperiodic solutions of Eqs. (7), (8) via Eq. (11). The variable s accounts for the deviation of the time dependence of the solution $\mathbf{v}$ from the assumed periodicity.

This simple procedure was already implemented directly [22] for an unsteady flow with a given periodicity by discretizing the time period by finite differences. Our investigation of the spectral decomposition of the cylinder wake [1] has, however, indicated that a spectral Fourier representation of the time behaviour is much more accurate and efficient as only a very small number of Fourier components appear to be relevant.

2.3. Fourier Decomposition of the Periodic Behaviour

The periodicity (12) of $\mathbf{u}(s, t, \cdot)$ in the variable t makes it possible to write $\mathbf{u}$ as a Fourier series,

$$\mathbf{u}(s, t, \cdot) = \sum_{n=-\infty}^{+\infty} \mathbf{c}_n(s, \cdot) e^{in\omega t}, \tag{13}$$

where $\omega = 2\pi/T$. The developed solution being real, the coefficients (which are functions of s and the spatial variables) of the development satisfy the relation:

$$\mathbf{c}_n(s, \cdot) = \overline{\mathbf{c}_{-n}(s, \cdot)}.$$

The Fourier decomposition (13) inserted into Eqs. (9) and (5) yields the following system of coupled equations:

$$\frac{\partial \mathbf{c}_n}{\partial s} + (in\omega - \nu\nabla^2)\mathbf{c}_n + \sum_{k=-\infty}^{+\infty} \mathbf{B}(\mathbf{c}_k, \mathbf{c}_{n-k}) = 0, \tag{14}$$

In more detail, if we introduce the Fourier decomposition of the pressure,

$$p(s, t, \cdot) = \sum_{n=-\infty}^{+\infty} d_n(s, \cdot) e^{in\omega t}, \tag{15}$$

Eq. (14) can be written as

$$\frac{\partial \mathbf{c}_n}{\partial s} + (in\omega - \nu\nabla^2)\mathbf{c}_n + \sum_{k=-\infty}^{+\infty} (\mathbf{c}_k \cdot \nabla) \cdot \mathbf{c}_{n-k} + \nabla d_n = 0, \tag{16}$$

where $\mathbf{c}_n$ satisfies the continuity equation

$$\nabla \cdot \mathbf{c}_n = 0. \tag{17}$$

As we have seen above the continuity equation is equivalent to the second term of the RHS of Eq. (6).

Equations (15)–(17) require an initial condition representing an inital guess of the behaviour over one period. The initial condition can be determined by physical and/or numerical considerations. In our case we shall test our method on the development of the Bénard–Von Kármán instability. The zeroth harmonic represents the mean value of the flow. At the onset of the instability it corresponds to the steady basic flow. The linear (infinitesimal) instationnarity corresponds to the solution of the linear instability problem. The linear theory yields harmonic oscillations with a given frequency ω and a given amplification rate γ. The spatial dependence is defined by the (normalized) unstable eigenfunction ϕ [1]. As a result a physical initial condition consists in setting all but the first harmonic $\mathbf{c}_1 = \overline{\mathbf{c}_{-1}}$ to zero, the first harmonic having the initial behaviour,

$$\mathbf{c}_1(s, \cdot) \underset{s \to 0}{\sim} a e^{\gamma s} \phi, \tag{18}$$

where a is a small factor determining the initial level of the perturbation of the basic flow. (It appears that a fairly arbitrary set of inital values of the Fourier components can be taken. The advantage of the physically correct initial condition is to reduce the numerical transients and to enable to follow the development of the instability from much lower levels than using classical direct solution methods.

The formulation presented in this section is strictly equivalent to the initial Navier–Stokes formulation (1), (2). In particular, even unperiodic flows, or flows having a period significantly different from that chosen in Eq. (12), satisfy Eqs. (13) and (14), the variable s accounting for the deviation from the assumed periodicity. This property is important for flows with self-generated periodicity where the period is not known a priori as well as for the treatment of transients. It enables us also to account for frequencies varying in space. It is nevertheless obvious that the accuracy and efficiency of the method will largely depend on how well the periodicity assumption (12) is satisfied. In what follows special attention will be paid to the optimization of the choice of the period T so as to minimize the s-derivative in Eqs. (9) and (14). If this can be done the accuracy of the time discretization becomes practically spectral.

3. NUMERICAL IMPLEMENTATION

3.1. Modification of the Time Marching Method

The numerical implementation of the proposed method was based on a modification of a finite-volume time marching resolution of the Navier–Stokes equations second-order accurate in both space and time developed by Braza *et al.* [13, 23]. The

second-order time discretization steps in the initial formulation can be summed up as

$$\frac{\mathbf{V}^* - \mathbf{V}^l}{\Delta t} + (\mathbf{V}^l \cdot \nabla)\frac{1}{2}(\mathbf{V}^* + \mathbf{V}^l) - \nu\nabla^2\frac{1}{2}(\mathbf{V}^* + \mathbf{V}^l) + \nabla P^l = 0, \tag{19}$$

$$\nabla^2 \phi = \nabla \cdot \mathbf{V}^*, \tag{20}$$

$$\mathbf{V}^{l+1} = \mathbf{V}^* - \nabla\phi, \tag{21}$$

$$P^{l+1} = P^l + \frac{\phi}{\Delta t}, \tag{22}$$

where $(\mathbf{V}, P)$ stands for the discrete version of $(\mathbf{v}, p)$ solution of the continuous problem at the time $t = l\Delta t$.

The time advancement in t is now replaced by a time advancement in s. Applying the time discretization (19) to (22) for Eqs. (16), (17) we obtain for a first-order formulation,

$$\frac{\mathbf{C}_n^{m+1} - \mathbf{C}_n^m}{\Delta s} + in\omega\mathbf{C}_n^{m+1} + \sum_{k=-\infty}^{k=+\infty}(\mathbf{C}_k^{m+1} \cdot \nabla)\mathbf{C}_{n-k}^{m+1} - \nu\nabla^2\mathbf{C}_n^{m+1} + \nabla D_n^{m+1} = 0, \tag{23}$$

or a second-order formulation,

$$\frac{\mathbf{C}_n^{m+1} - \mathbf{C}_n^m}{\Delta s} + in\omega\frac{1}{2}(\mathbf{C}_n^{m+1} + \mathbf{C}_n^m) + \sum_{k=-\infty}^{k=+\infty}(\mathbf{C}_k^{m+1} \cdot \nabla)\frac{1}{2}(\mathbf{C}_{n-k}^{m+1} + \mathbf{C}_{n-k}^m) - \nu\nabla^2\frac{1}{2}(\mathbf{C}_n^{m+1} + \mathbf{C}_n^m) + \nabla D_n^{m+1} = 0, \tag{24}$$

where $\mathbf{C}_n^m$ and D_n^m stand for the discrete version of $\mathbf{c}_n$ and d_n at the time $s = m\,\Delta\,s$. To solve Eq. (23) or (24), together with

$$\nabla \cdot \mathbf{C}_n^{m+1} = 0, \tag{25}$$

we introduce the intermediate iteration procedure,

$$\frac{\mathbf{C}_n^* - \mathbf{C}_n^j}{\Delta h} + \frac{\mathbf{C}_n^* - \mathbf{C}_n^m}{\Delta s} + in\omega\mathbf{C}_n^* + \sum_{k=-\infty}^{k=+\infty}(\mathbf{C}_k^j \cdot \nabla)\mathbf{C}_{n-k}^* - \nu\nabla^2\mathbf{C}_n^* + \nabla D_n^j = 0, \tag{26}$$

or

$$\frac{\mathbf{C}_n^* - \mathbf{C}_n^j}{\Delta h} + \frac{\mathbf{C}_n^* - \mathbf{C}_n^m}{\Delta s} + in\omega\frac{1}{2}(\mathbf{C}_n^* + \mathbf{C}_n^m) + \sum_{k=-\infty}^{k=+\infty}(\mathbf{C}_k^j \cdot \nabla)\frac{1}{2}(\mathbf{C}_{n-k}^* + \mathbf{C}_{n-k}^m) - \nu\nabla^2\frac{1}{2}(\mathbf{C}_n^* + \mathbf{C}_n^m) + \nabla D_n^j = 0, \tag{27}$$

$$\nabla^2\Phi_n = \nabla \cdot \mathbf{C}_n^*, \tag{28}$$

$$\mathbf{C}_n^{j+1} = \mathbf{C}_n^* - \nabla\Phi_n, \tag{29}$$

$$D_n^{j+1} = D_n^j + \frac{\Phi_n}{\Delta s}. \tag{30}$$

Equation (26) or (27) is discretized by a second-order finite volume method in space and solved by an ADI method. Δh is chosen to optimize the ADI algorithm. For each j-step, one ADI sweep in both space directions is carried out in Eq. (26) or (27) and Eq. (28) is solved by several iterations of an ADI Laplace solver to obtain a divergenceless next approximation by Eq. (29). The $(j + 1)$th pressure correction is given by Eq. (30). At convergence,

$$\lim_{j\to\infty}\mathbf{C}_n^j = \mathbf{C}_n^{m+1},$$

we thus obtain the solution of Eq. (23) or (24).

3.2. Spatial Discretization

The spatial discretization is based on a finite-volume method applied to the Navier–Stokes equations written in their conservative form and integrated over an elementary volume [13, 23]. Primitive variables (u, v, p) are discretized on staggered meshes to overcome the pressure checkerboard problem. A centered discretization of the diffusion term yields a second-order space accuracy. Dirichlet boundary conditions are applied at the inlet as well as at the side walls and Neumann boundary conditions $\partial\mathbf{c}_n/\partial x = 0$ at the outlet. The configuration and the boundary conditions are presented in Fig. 1. The (102×32) point grid used for the simulations is shown in Fig. 2.

3.3 Period Correction

We apply our method to an afterbody wake. The oscillations of the wake being self-generated and their period varying in time, the accuracy is maximized by implementing a period correction algorithm to adjust the instantaneous period value. This can be done by minimizing the s-derivative which leads to a practically spectral time accuracy.

The correction is based on the minimizing of the angular velocity $\Delta\omega$ of the fundamental harmonic of the v-velocity

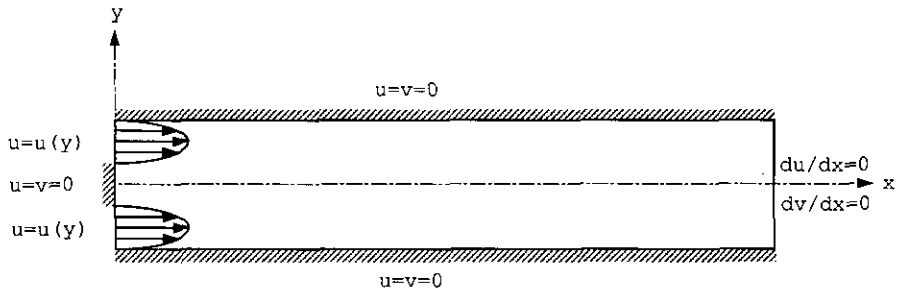

FIG. 1. Domain of calculation and boundary conditions.

denoted V_1. (In what follows we denote by U_n, V_n the components of each Fourrier mode $\mathbf{c}_n \equiv (U_n, V_n)$.) The phase variation of the $n = 1$ Fourier component of the transverse velocity in the complex plane is a measure of $\Delta\omega$ defined as the difference between the true value ω_o of the angular velocity and the approximate one $\omega = \omega_o - \Delta\omega$. As a result, at each s-iteration the angular velocity correction can be calculated as

$$\Delta\omega + \frac{\theta_1^{m+1} - \theta_1^m}{\Delta s}, \tag{31}$$

θ_1^m being the argument of $\mathbf{C}_1$ at time $s = m\Delta s$. The value of $\Delta\omega$ calculated in Eq. (31) is used to update ω, so that the value $\omega + \Delta\omega$, instead of ω, is used in Eq. (23) or (24) at the next s-step.

4. NUMERICAL RESULTS

We have tested the presented method on the simulation of the development of the Bénard–von Kármán instability in the afterbody wake described in Section 3.2 near the instability threshold. The Reynolds number is based on the bulk velocity ($U_b = 1$) and the width of the afterbody ($D_o = \frac{1}{3}$). The critical Reynolds number has been found ≈ 85 in this case and the value Re = 90 has been retained for the flow simulation. The length and velocity scales are nondimensionalised with respect to the domain width $L = 1$ and the bulk velocity $U_b = 1$, respectively.

First, we have determined the influence of the time step on the cost of the calculation and proved the existence of an optimum. Second, we have tested the behaviour of the scheme using a constant value for the angular velocity ω. Third, we have introduced the angular velocity correction and proved its efficiency. Finally, we have applied this scheme to the complete simulation of the growth of the instability up to the saturation by using an approximation with only three leading harmonics.

4.1. Optimisation of the CPU-Time

In order to optimize the method, it is interesting to search for the time step Δs that minimizes the CPU-time. The estimates are performed in the transient phase of the flow and, apart from the mean flow, we keep only the first harmonic.

For each value of Δs considered here, one hundred internal iterations (26) through (30) are carried out. Then the number of internal iterations required for reaching a certain fixed accuracy is determined. The accuracy criterion is based on the ratio between the residual ε_1 of the conservation equation for $\mathbf{C}_1$ and $|\partial\mathbf{C}_1/\partial s|$.

$$\varepsilon_1 / \left|\frac{\partial \mathbf{C}_1}{\partial s}\right| \leq 10^{-3}.$$

We can thus determine the CPU-time necessary for simulating a given s-interval (0.4 time units in this case) with a fixed accuracy from the CPU-time for a single time step in terms of the number of internal iterations.

The results for our two different schemes are presented in Fig. 3. The solid line corresponds to the second-order accurate scheme, the dashed one for the first-order accurate one. These results prove the existence of an optimal Δs for each type of scheme as well as the superiority of the second-order accurate scheme from this point of view.

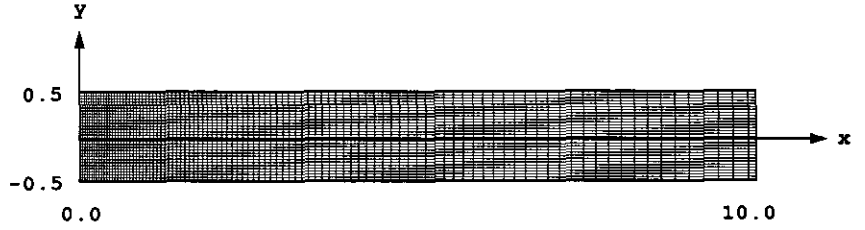

FIG. 2. (102 × 32) points grid used for the simulation.

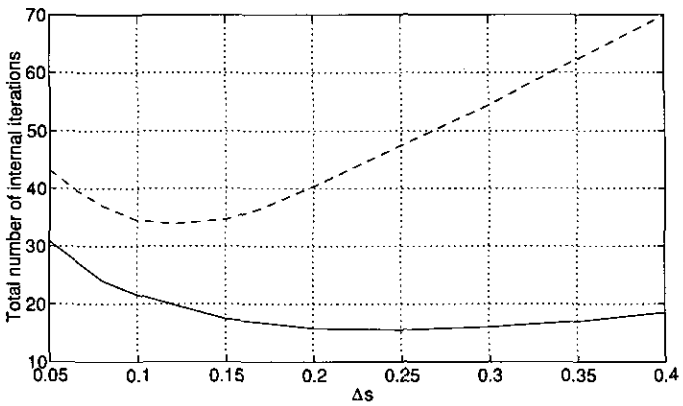

FIG. 3. CPU-time in terms of the number of internal iterations necessary to simulate an s-interval of length 0.4 with a 10^{-3} accuracy of the term $\partial \mathbf{C}_l/\partial s$, depending on the time step Δs and the type of the scheme: first-order accurate (dashed line); second-order accurate (solid line).

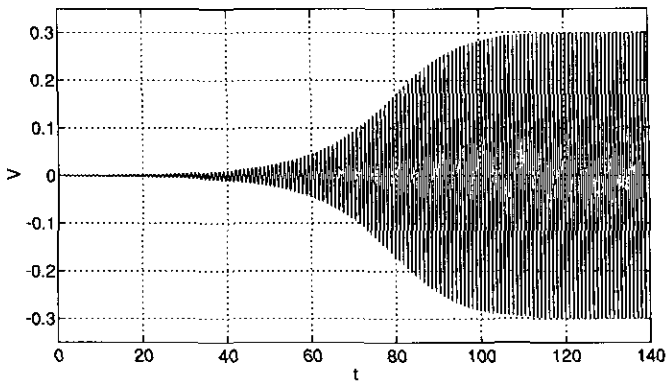

FIG. 4. Time evolution of the transverse velocity V for the calculation with a standard time marching scheme.

4.2. Transient Flow Simulated with a Standard Scheme

In this section, we present the simulation of the transients with a standard second-order accurate finite difference time marching scheme combined with finite volume space discretization. Two steps have been tested $\Delta t = 10^{-2}$ and $\Delta t = 10^{-3}$ ($\approx$1000 time steps per period). We recall that the results are made dimensionless using the width $L = 1$ of the channel and the bulk velocity $U_b = 1$. The reference time is thus $L/U_b = 1$.

The results obtained with $\Delta t = 10^{-2}$ have proved that the low time accuracy of this calculation has a large influence on the behaviour of the transients. Indeed, the amplification rate is twice as large as that obtained from the calculation with $\Delta t = 10^{-3}$. As a consequence, the critical Reynolds number determined with $\Delta t = 10^{-2}$ is found to be as low as 76 and the saturation value of the transverse velocity V is found to be 40 % larger than that obtained with $\Delta t = 10^{-3}$.

The results of the calculation with $\Delta t = 10^{-3}$ are shown in Figs. 4–6. Figure 4 shows the time evolution of the transverse velocity V at the point (1.04, 0.0) on the axis of symmetry of the domain. The envelope of this signal is presented (Fig. 5) in cartesian and logarithmic coordinates to show the exponential growth of V. The time evolution of the angular velocity ω is given in Fig. 6. We conclude that the instability characteristics depend strongly on the accuracy of the time discretization. The levels of the residuals obtained with $\Delta t = 10^{-3}$ ($>10^{-3}$) are indicative of a still unsufficient precision, however, the computing costs of a still finer time-resolution would have been prohibitive.

These results have to be compared to those obtained with the spectral version of the code.

4.3. Flow at Saturation without Period Correction

The solution obtained at saturation with the standard time marching scheme with $\Delta t = 10^{-2}$ is used to estimate the period of the flow and to calculate the Fourier coefficients for the initial condition for the spectral code. The Fourier decomposition is restricted to the harmonics 0, 1, and 2 and we chose the first-order accurate s-scheme version for which the optimal value of Δs was found to be $\approx$0.1. In the following sections, U_n and V_n are, respectively, the x and y-components of $\mathbf{C}_n$.

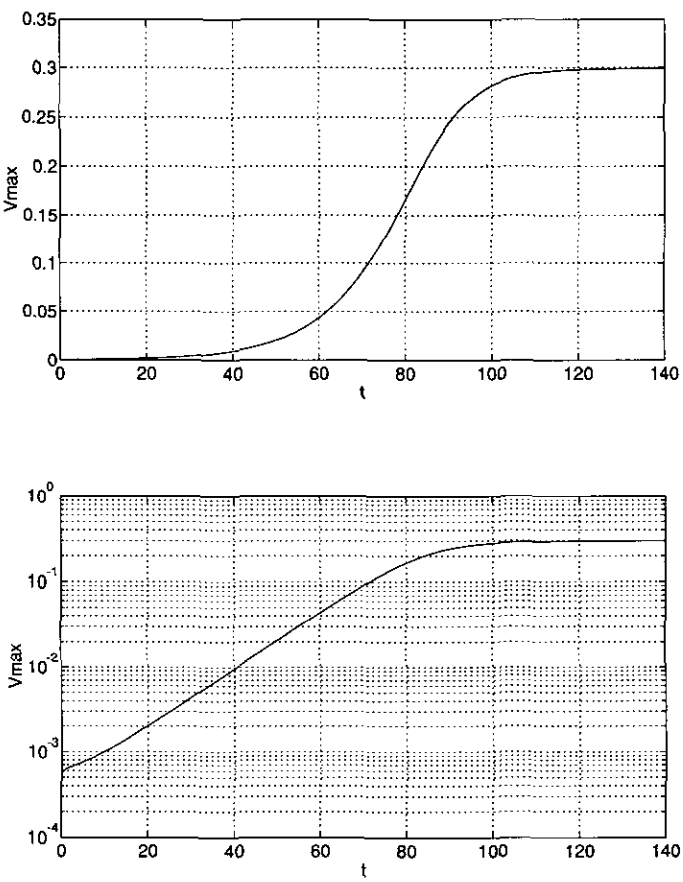

FIG. 5. Time evolution of the envelope of the transverse velocity V for the calculation with a standard time marching scheme.

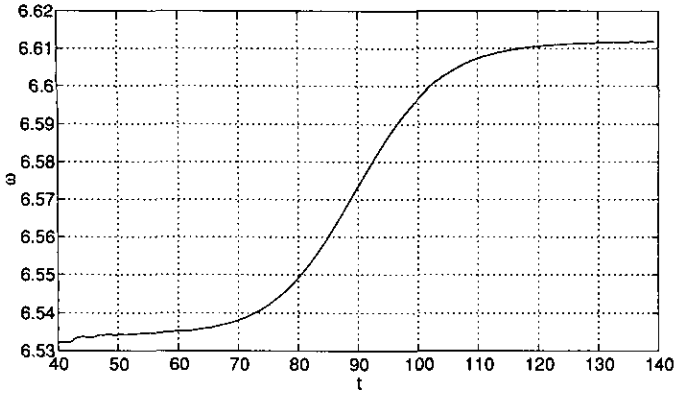

FIG. 6. Time evolution of the angular velocity ω for the calculation with a standard time marching scheme.

Because of the differences in the time discretization between both methods, the value of the angular velocity ω obtained from the time marching calculation does no longer represent the saturation value ω_{sat} of the angular velocity for the new approximation. As a consequence, the Fourier components are not steady. They reach a limit cycle at which the $n = 1$ Fourier component rotates in a complex plane with the constant angular velocity $\Delta\omega = \omega_{sat} - \omega$ and evolves according to the following relationship:

$$\mathbf{C}_1(s, x) = |\mathbf{C}_1(x)|e^{i\Delta\omega s}.$$

Figures 7 and 8 represent the time evolution of the absolute value of the x-component U_1 at the point (1.06, −0.017) and of the y-component V_1 at the point (1.04, 0.0) on the axis of symmetry. We first note that, indeed, a limit corresponding to the saturation is reached. U_1 reaches a limit cycle represented in the complex plane by a circle with radius $|U_1|$ and characterized by the constant angular velocity $\Delta\omega$ (Fig. 9).

Finally, in Fig. 10 we note that the residual ε_1 of the conservation equation for U_1 can not be reduced under a certain limit (3.10^{-6}) because of the non negligible value of $\partial U_1/\partial s$ and of the first-order accuracy of the s-time marching scheme. A better accuracy is achieved by eliminating the s-variation of $\mathbf{C}_n$ using the angular velocity correction described below.

4.4. Angular Velocity Correction for a Flow at Saturation

The conditions of this calculation are strictly the same as in the previous section but the procedure to correct the angular velocity is now introduced into the scheme.

We first note, in Fig. 11, that the limit cycle disappears to be replaced by a limit point in the complex plane due to the the complex Fourier coefficient reaching a steady state. In the same time, we observe, in Figs. 12 and 13, an exponential decay for $|\partial U_1/\partial s|$ as well as for $\Delta\omega$. The residual ε_1 of the

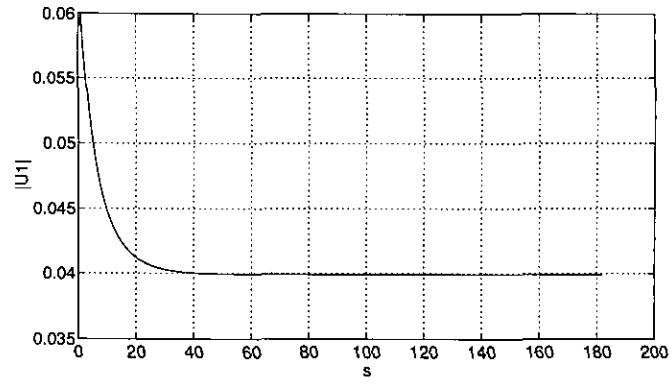

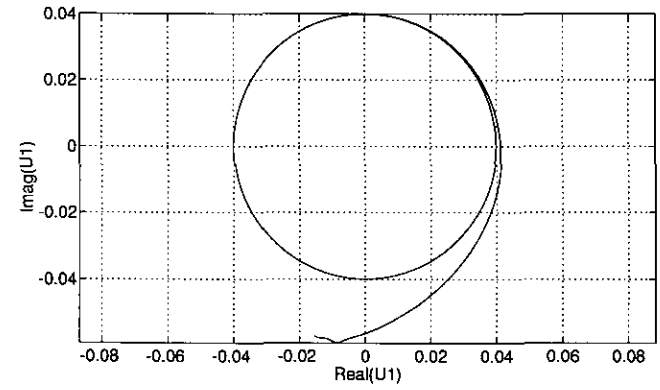

FIG. 7. Time evolution of $|U_1|$ and of U_1 in the complex plane for the calculation with constant angular velocity ω.

conservation equation for U_1 is now ten times smaller than in the previous calculation with a constant angular velocity (see Figs. 10 and 12).

Because $\Delta\omega$ is now reduced to zero, the accuracy of the solution does not depend anymore on Δs in the same way as the accuracy of the solution of a steady flow does not depend on Δt. Then, the spectral time accuracy is reached and the overall precision of the solution depends just on the number of the calculated harmonics and on the space discretization. At the convergence, the correct angular velocity ω_{sat} of the flow is obtained as shown in Fig. 14.

4.5. Validation of the Method by Simulation of the Transients of the Instability

4.5.1. *Quantitative Results and Their Physical Consistence*

The simulation of the saturation of the instability due to the nonlinear effects is now performed with harmonics 0, 1, and 2 kept in the Fourier expansion (13). This low number of harmonics taken into account was justified by the fact that acounting for higher harmonics was found to change the saturation level of the fundamental by less than 0.1% (see Table I). The initial condition is chosen such that its oscillation amplitude

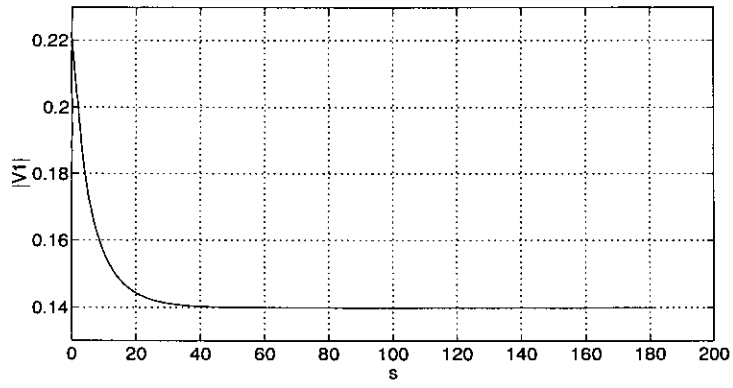

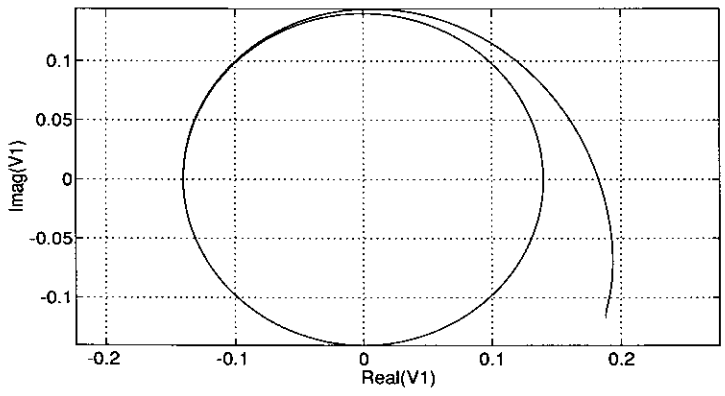

FIG. 8. Time evolution of $|V_1|$ and of V_1 in the complex plane for the calculation with constant angular velocity ω.

corresponds to 10^{-6} of the expected saturation value for $\mathbf{C}_1$, $\mathbf{C}_2$ being set equal to zero as suggested in the Section 2.3. By this mean, the numerical transients are short compared to the physical ones and from the time $s = 10$, they do not contaminate the solution anymore. As shown in the following figures, all the characteristic aspects of transients are obtained and correspond to a Hopf bifurcation [1].

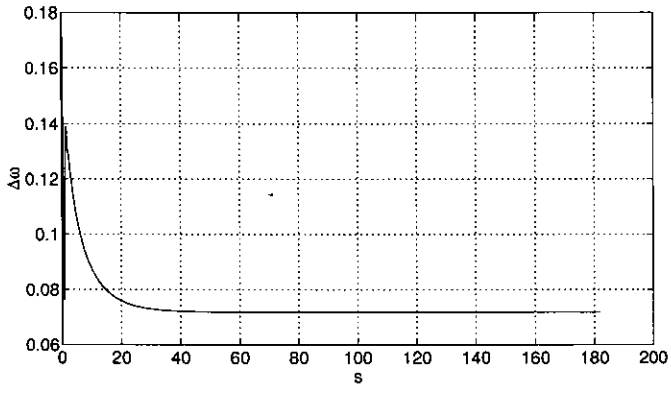

FIG. 9. Time evolution of $\Delta\omega$ for the calculation with constant angular velocity ω.

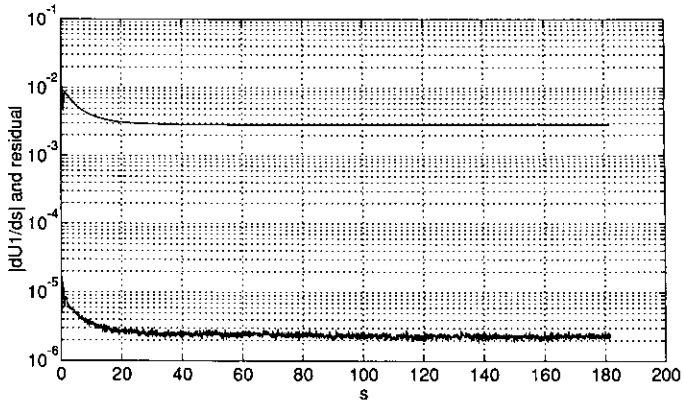

FIG. 10. Time evolution of $|\partial U_1/\partial s|$ (solid line) and of the residual ε_1 of the conservation equation for U_1 (dashed line) for the calculation with constant angular velocity ω.

The angular velocity increases by a few percent to reach a constant value at the saturation (Fig. 15). The linear relationship between the angular velocity and $|U_1|^2$ is obtained in agreement with the theory [1, 8, 12] (Fig. 16). In the same way, this theory also predicts a linear relationship between $(\partial|U_1|/\partial s)/|U_1|$ and $|U_1|^2$ that is obtained with good agreement (Fig. 17).

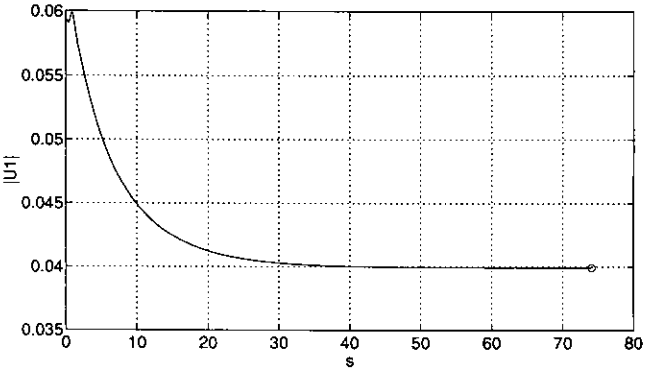

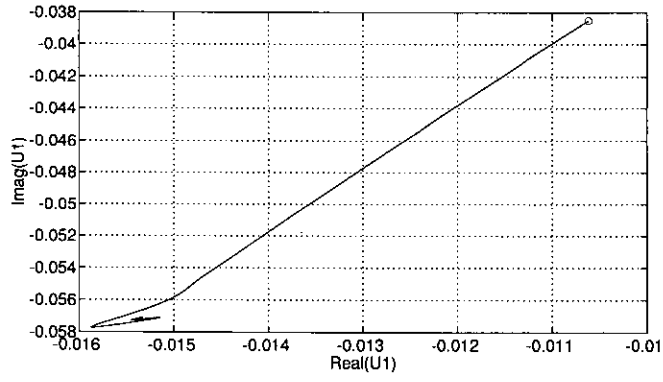

FIG. 11. Time evolution of $|U_1|$ and of U_1 in the complex plane for the calculation with period correction.

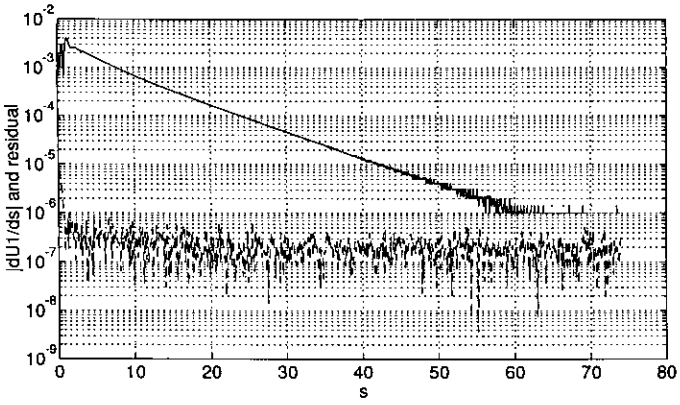

FIG. 12. Time evolution of $|\partial U_1/\partial s|$ (solid line) and of the residual ε_1 (dashed line) for the calculation with period correction.

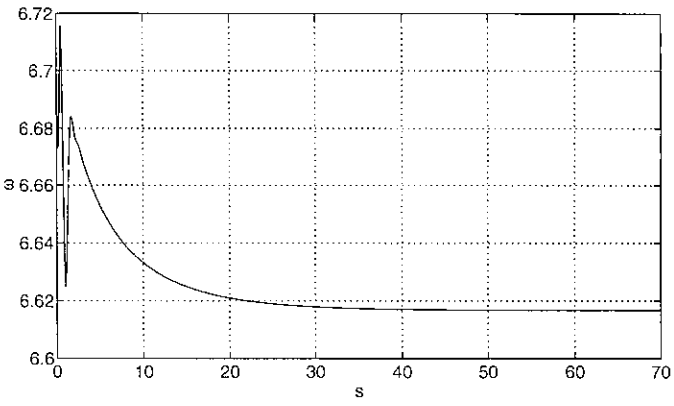

FIG. 14. Time evolution of ω for the calculation with period correction.

$|U_1|$ has first an exponential growth before reaching the saturation shown in Fig. 18. Its saturation value is small because the point (10.6, 0.483) is close to the axis of symmetry.

$|V_1|$, observed at the point (10.4, 0.5), increases by four orders of magnitude to reach finally its saturation value ≈0.14. The logarithmic coordinates put into light the exponential growth of the instability. The slope of the linear part of the logarithmic plot in Fig. 19 gives the amplification rate $\gamma = 0.0698$.

The second harmonic U_2 has qualitatively the same behaviour as U_1, except that it increases by eight orders of magnitude in the same time interval (Fig. 20). This is in agreement with the fact that its amplification rate should be 2γ [1].

According to the theory [1], the nonlinear correction of the mean value should have the same amplification rate 2γ as the second harmonic. To see this, we subtract the unperturbed flow (the mean flow $U_o \approx 0.1742$ before the development of the instability). Indeed, Fig. 21 is in agreement with this theoretical result.

The relative numerical error on the angular velocity ω (Fig. 22) is obtained by comparing $\Delta\omega$ defined by the relation (31) to $\omega_{sat} - \omega_i$, where ω_i is the initial value of the angular velocity of the infinitesimal perturbation and ω_{sat} is its saturation value.

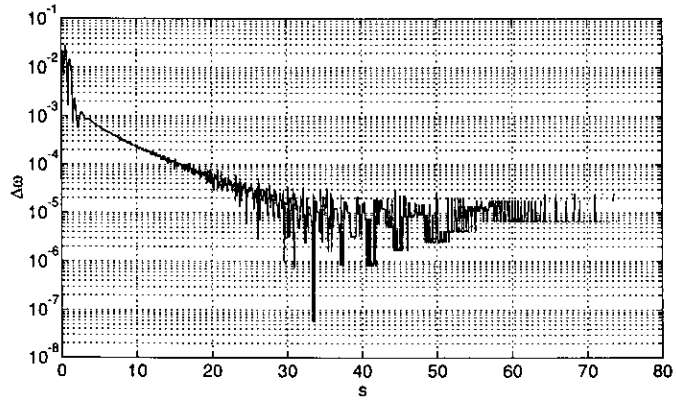

FIG. 13. Time evolution of $\Delta\omega$ for the calculation with period correction.

This relative error does not exceed 0.4%. This accuracy is far higher, compared to what has been obtained with standard methods of analysis used in [1].

The residual ε_1 of the conservation equation for U_1 remains smaller than 2×10^{-7}. The error on $|\partial U_1/\partial s|$ is then less than 0.01% as can be seen in Fig. 23. From the time $s = 170$, the modulus of $\partial U_1/\partial s$ decreases and its value at the time $s = 250$ is of the same order of magnitude as ε_1 because saturation is reached.

The value of $|\partial U_1/\partial s|$ is rather accurately equal to $\partial|U_1|/\partial s$ as can be seen from

$$\frac{\partial U_1}{\partial s} = \frac{\partial |U_1|}{\partial s} e^{i\Delta\omega s} + i\Delta\omega |U_1| e^{i\Delta\omega s} \tag{32}$$

if we take into account the values of $|\partial U_1/\partial s|$, $|U_1|$ and $\Delta\omega$ from Figs. 23, 18, and 22.

4.5.2. *Comparisons with the Results of the Standard Time Marching Scheme*

Comparisons have to be made with the results obtained with the standard time marching scheme (STM scheme) with $\Delta t = 10^{-3}$ in Section 4.2. The results of the comparison are assembled in Table II. We first note that the amplification rate $\gamma \approx 0.077$ is 10.3% higher than the amplification rate of V_1 obtained with the spectral calculation. According to [6], γ should be linearly dependent on the difference $Re - Re_c$ (Re_c is the critical Reyn-

TABLE I

Comparisons of the Saturation Levels of the v-Velocity of the Fundamental Harmonic for Varying Number j of Harmonics Taken into Account

j	1	2	3	4
$\lvert c_{1,u}^{(j)} - c_{1,u}^{(j+1)}\rvert / c_{1,u}^{(5)}\rvert$	1.1710^{-2}	6.7010^{-4}	2.7010^{-5}	1.7910^{-6}
$\lvert c_{1,v}^{(j)} - c_{1,v}^{(j+1)}\rvert / c_{1,v}^{(5)}\rvert$	1.5610^{-2}	5.5510^{-4}	1.6210^{-5}	6.2310^{-7}

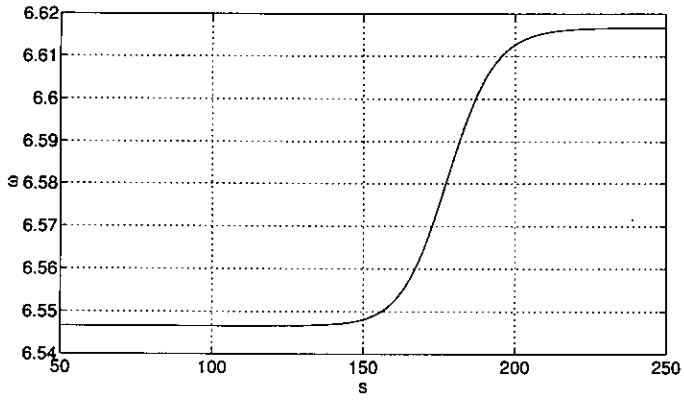

FIG. 15. Time evolution of the angular velocity ω.

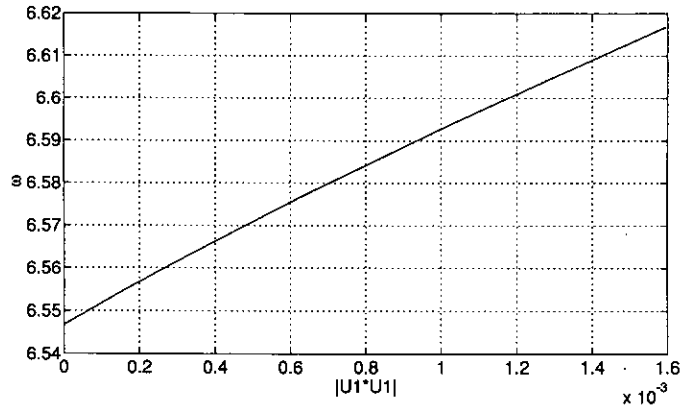

FIG. 16. Linear dependence of ω on $|U_1^2|$.

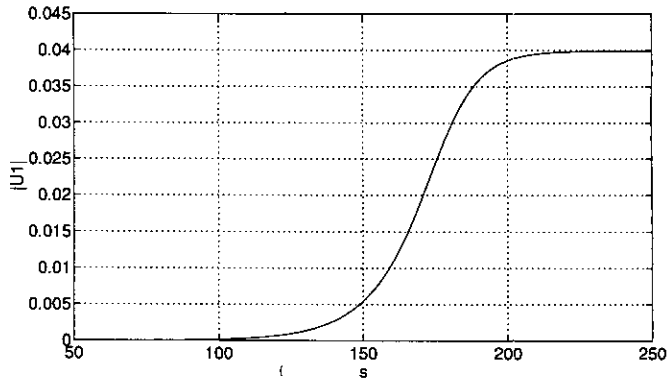

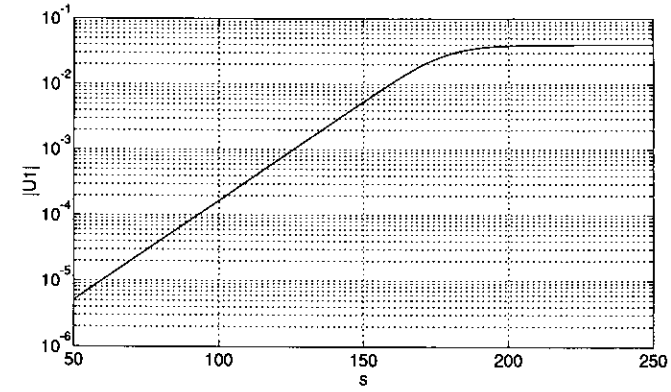

FIG. 18. Time evolution of $|U_1|$ at the point (10.6, −0.017).

olds number of the flow). We thus deduce that the critical Reynolds number obtained from the STM calculation is lower than the spectral one. This is consistent with the saturation value $V_{max} \approx 0.3$. According to the relation (13), the corresponding Fourier coefficient is 0.15. This value is 7% higher than the value of $|V_1| \approx 0.14$ obtained from the spectral calculation.

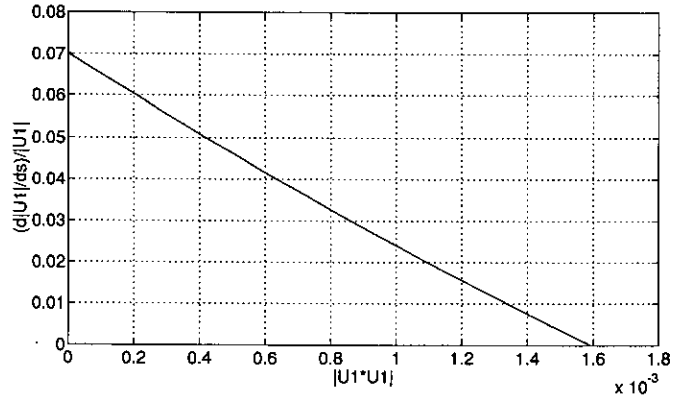

FIG. 17. Linear dependence of $(\partial|U_1|/\partial s)/|U_1|$ on $|U_1^2|$.

The standard time marching scheme with 100 time steps per period yielded a saturation amplitude of as much as 0.22. Alone these three results indicate the obtained increase of the time discretization accuracy.

We performed an additional spectral calculation at the saturation using six leading harmonics (0 through 5). We observe that the saturation value for V_1 is unchanged and the saturation

TABLE II

Comparison of the Computing Costs and of the Residuals of the Standard Time-Marching Method and of the Present Spectral Time Discretization Method

	STM scheme	Spectral scheme	Difference
Mesh	102 × 32	102 × 32	Identical
Space discretization	Finite volume	Finite volume	Identical
Amplification rate γ	0.077	0.0698	10%
Saturation value $\|V_1\|$	0.150	0.140	7%
$\omega_{sat} - \omega_i$	0.078	0.070	11%
Residual ε	4×10^{-3}	2×10^{-7}	20000
CPU-time (hours)	127	53	140%
Memory	4.5 Mo	6.7 Mo	49%

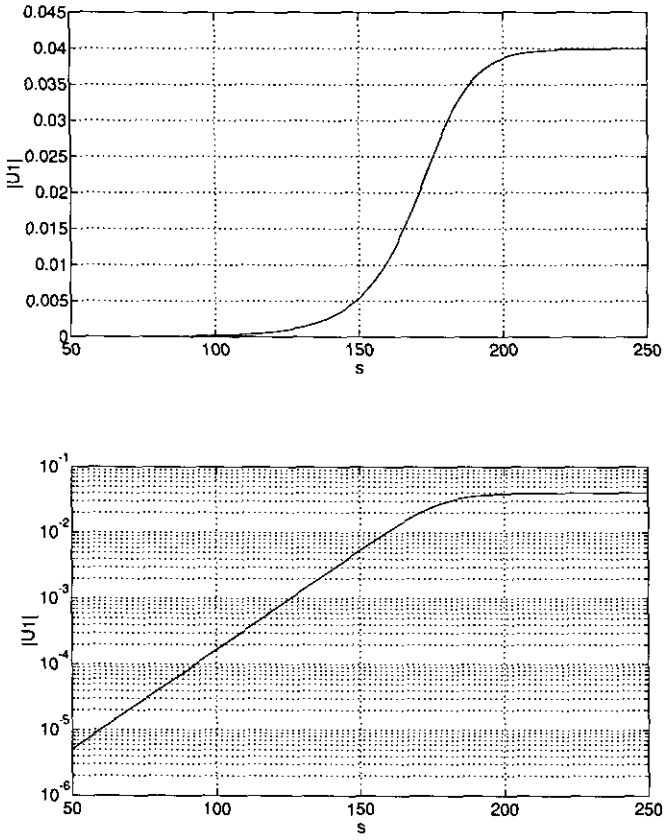

FIG. 19. Time evolution of $|V_1|$ at the point (1.04, 0.0).

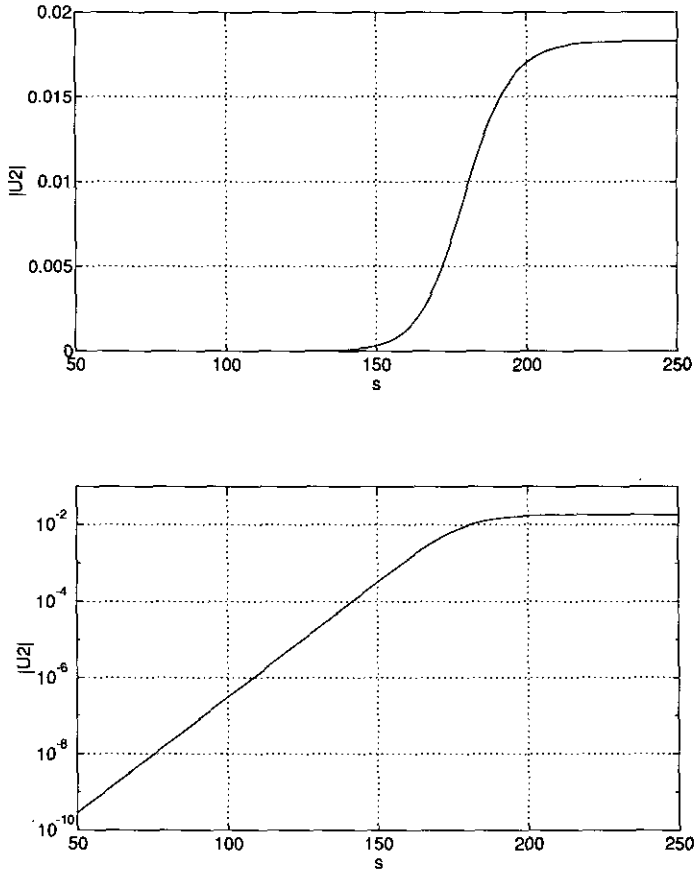

FIG. 20. Time evolution of the second harmonic $|U_2|$.

values for V_3 and V_5 are respectively 2×10^{-3} and 3×10^{-5}. From this, we can conclude that the difference between the saturation values of V for the STM scheme and V_1 for the spectral scheme is not related to the number of harmonics taken into account in the spectral calculation (see Table I).

Because the mesh and the spatial discretization are the same for both calculations, these differences have to be attributed to the differences in the time discretization. It appears that despite the small time step $\Delta t = 10^{-3}$, the time accuracy of the STM scheme is significantly lower than the time accuracy of the spectral scheme. The residual of the u-equation for the STM scheme is equal to 4×10^{-3}, i.e., 1% of the diffusion term which is the smallest term of this equation. The equivalent residual for the spectral scheme is less than 2×10^{-7}, i.e., 2×10^4 times smaller than the STM residual.

The CPU-time required for the STM calculation on a Silicon Graphics IRIS 4D/320 GTX computer was found to be 127 h for a 140 time units duration, whereas it was only 53 h for the spectral calculation. For the presented case, the required memory is 4.5 Mo for the STM scheme and 6.7 Mo for the spectral one. (We focussed rather to the improvement of the accuracy than to the CPU-time reduction.)

5. CONCLUSIONS

We have not tried to present a complete well-balanced simulation method with the same discretization accuracy, relative to the time and space; neither have we taken into account a sufficient number of harmonics. The point was to focus on the time discretization method. The results show that it can be made extremely accurate and efficient. For the presented case of the unstable wake, it appeared that, in addition, the method provides direct access for a number of characteristics of the instability transients difficult to obtain by ordinary time marching techniques such as the time evolution of the angular velocity.

In combination with a more accurate spatial discretization, the method may become a useful numerical and theoretical tool for the treatment of any instabilities presenting the characteristics of the Hopf bifurcation such as those in wakes and jets, on free surfaces and interfaces. The method is potentially appropriate to any type of flow with a dominant periodicity.

The presented example of unstable wake exploits the ability of the method to separate slow and rapid time scales. Another possiblity is presently under investigation. In periodic turbulent

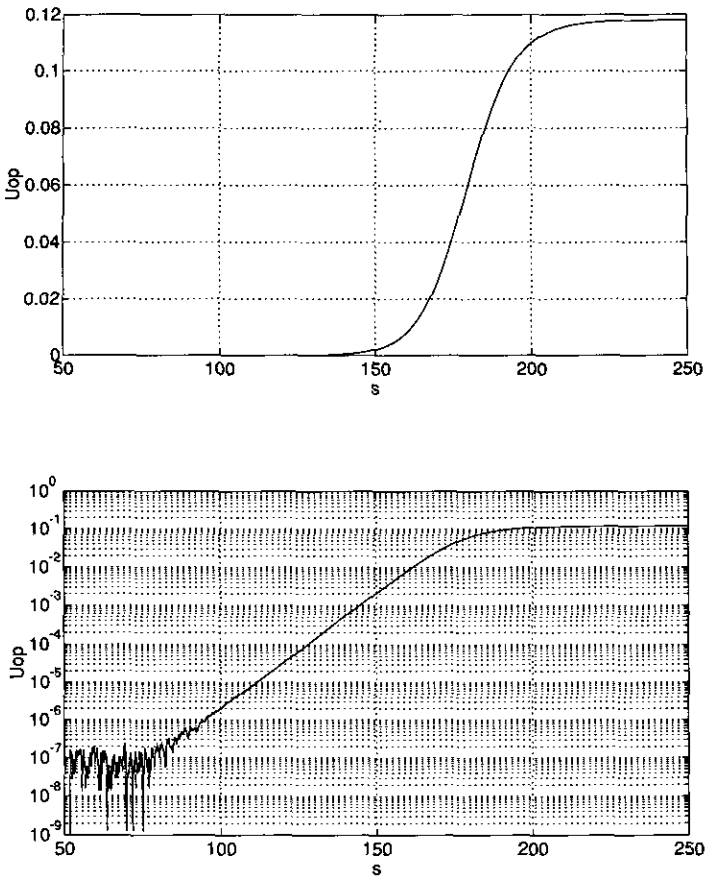

FIG. 21. Time evolution of the perturbation U_{op} of the mean flow.

wakes slow periodic oscillations of large scale vortices coexists with a rapid motion of small scale turbulent structures. Standard turbulence models aim at modelling the latter and at accounting for the former by standard time marching schemes. This approach appears to be rather difficult (see Ref. [21]). The spectral time discretization allows us to consider the problem from a completely different viewpoint. The introduction of the Fourier components reduces the unsteady problem to a steady formulation for which turbulence modelling techniques analogous to those for steady turbulent flows can be used and the transfer of energy from the mean flow through the harmonics to the turbulent structures can be taken into account explicitly.

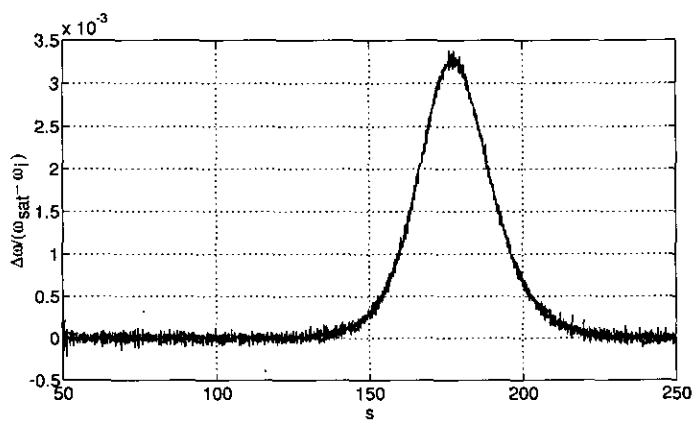

FIG. 22. Time evolution of the ratio $\Delta\omega/(\omega_{sat} - \omega_i)$.

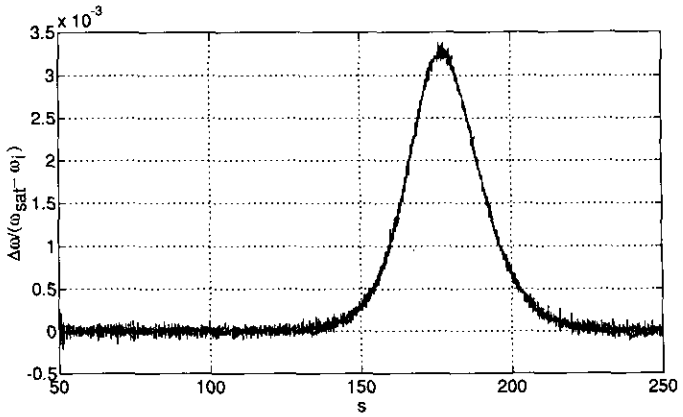

FIG. 23. Time evolution of $|\partial U_i/\partial s|$ (solid line) and of the residual ε_i of the conservation equation for U_i (dashed line).

ACKNOWLEDGMENTS

Gilles Carte wishes to thank the Electricité de France Service RNE-TTA for the three years Ph.D. Grant T37 L09 to support this work. Jan Dušek thanks the French Ministère de l'Enseignement Supérieur et de la Recherche for the visiting professor's position at the Institut de Mécanique Statistique de la Turbulence in Marseilles in the framework he carried out the present work.

REFERENCES

1. J. Dušek, P. Le Gal, and Ph. Fraunié, *J. Fluid Mech.* **264**, 59 (1994).
2. K. Stewartson and J. T. Stuart, *J. Fluid Mech.* **48**, 529 (1971).
3. F. P. Bertolotti, Th. Herbert, and P. R. Spalart, *J. Fluid Mech.* **242**, 441 (1992).
4. S. Raghu and P. A. Monkewitz, *Phys. Fluids A* **3**, 501 (1991).
5. P. Manneville, *Dissipative Structures and Weak Turbulence* (Academic Press, San Diego/London, 1990).
6. C. Mathis, M. Provansal, and L. Boyer, *J. Fluid Mech.* **182**, 1 (1987).
7. P. J. Strykowski and K. R. Sreenivasan, *J. Fluid Mech.* **218**, 71 (1990).
8. L. D. Landau and F. M. Lifschitz, *Fluid Mechanics, Course of Theoretical Physics*, Vol. 6. (Pergamon, Elmsford, NY, 1959).
9. S. Goujon-Durand, P. Jenffer, and J. E. Wesfreid, *Phys. Rev. E* (1994).
10. J. Dušek and Ph. Fraunié, in *Proceedings, Symposium on Application of Direct and Large Eddy Simulation to Transition and Turbulence, Chania, Crète, 18–21 avril 1994.*
11. G. E. Karniadakis and G. S. Triantafyllou, *J. Fluid Mech.* **238**, 1 (1992).
12. T. Leweke and M. Provansal, *J. Fluid Mech.*, submitted.
13. M. Braza, P. Chassaing, and H. Ha Minh, *J. Fluid Mech.* **165**, 79 (1986).
14. J. C. F. Pereira and J. M. M. Sousa, *J. Comput. Phys.* **106**, 14 (1993).
15. J.-L. Guermond, S. Huberson, and W.-Z. Shen, *J. Comput. Phys.* **108**, 343 (1993).
16. C. Liu and Z. Liu, *J. Comput. Phys.* **106**, 92 (1993).
17. W. D. Henshaw, *J. Comput. Phys.* **113**, 13 (1994).

18. H. D. Nguyen and J. N. Chung, *J. Comput. Phys.* **104**, 303 (1993).

19. Y. P. Marx, *J. Comput. Phys.* **112**, 182 (1994).

20. J. B. Perot, *J. Comput. Phys.* **108**, 51 (1993).

21. R. Franke and W. Rodi, in *Proceedings, Eighth Symp. on Turbulent Shear Flows, Munich, 1991*; H. Ha Minh, J. R. Viegas, M. W. Rubesin, D. D. Vandromme, and P. Spalart, in *Proceedings, Turbulent Shear Flow 7, Stanford, 1989*, M. Kato and B. E. Launder, TDF/92/13, UMIST, 1992 (unpublished).

22. G. Carte, Ph. Fraunié, and Ph. Dussouillez, in *Proceedings, Sixth International Symposium on Unsteady Aerodynamics, Aeroacoustics and Aeroelasticity of Turbomachines and Propellers, University Notre Dame, Sept. 15–19, 1991.*

23. G. Jin and M. Braza, *J. Comput. Phys.* **107**, 239 (1993).